

Evidence of Memory Effects in the Dynamics of Two-Level System Defect Ensembles Using Broadband, Cryogenic Transient Dielectric Spectroscopy

Qianxu Wang,^{1,2} Sara Magdalena Gómez,^{1,2} Juan S. Salcedo-Gallo,² Roy Leibovitz,² Jake Freeman,^{3,2} Salil Bedkihal,² and Mattias Fitzpatrick^{1,2,*}

¹Department of Physics and Astronomy, Dartmouth College, 6127 Wilder Laboratory, Hanover, New Hampshire 03755, USA

²Thayer School of Engineering, Dartmouth College, 15 Thayer Drive, Hanover, New Hampshire 03755, USA

³Department of Physics, Middlebury College, Middlebury, Vermont 05753, USA

(Dated: June 12, 2025)

Two-level system defects (TLSs) in dielectrics are believed to be the primary source of decoherence in superconducting circuits. However, the precise origin of these defects, including their atomistic morphology, frequency distributions, and dipole moments, remains relatively unexplored. A significant reason for this lack of understanding is that TLS defects are currently probed with resonators or qubits that require complex multi-stage fabrication processes. These probes are packaged, cooled in a dilution refrigerator, and measured to infer their corresponding coherence times. However, even frequency-tunable probes only gather information about TLS defects within their mode volume and a narrow bandwidth around their resonance frequency. As a result, a detailed understanding of the atomistic origins of TLS defects in isolated materials and interfaces is currently lacking, making it challenging to design the next generation of superconducting devices and dielectric materials from first principles. *Here, we introduce a novel approach that enables probing the cryogenic dielectric response of TLS defect ensembles using a broadband 3D waveguide. This technique provides evidence of memory effects in the dynamics of TLS defect ensembles that may enable the extraction of critical information about the origins of the underlying TLS defects and their interactions.* Importantly, this novel spectroscopy technique can be used at all stages of fabrication and ultimately inform mitigation strategies to reduce the impact of TLS defects on superconducting circuits. As a result, this technique will help usher in a new understanding of the atomistic origin of TLS defects, which will have profound consequences for quantum information science and the broader materials science community.

I. INTRODUCTION

Two-level system (TLS) defects are essential in understanding anomalous low-temperature properties of disordered solids, and they play a critical role in limiting the coherence of quantum technologies such as superconducting qubits and resonators. At low temperatures, many amorphous solids exhibit a thermodynamic behavior that deviates significantly from the predictions of Debye theory, which describes the specific heat of crystalline materials as scaling with T^3 . In contrast, experiments in the early 1970s revealed that glassy materials display a nearly linear temperature dependence of the specific heat at cryogenic temperatures [1]. To explain this anomalous behavior, Anderson, Halperin, and Varma [2], and independently Phillips [3], introduced the standard tunneling model (Fig. 1a). This model posits that structural disorder in dielectrics can give rise to atoms or groups of atoms residing in effective double-well potentials, allowing for quantum tunneling between two nearly degenerate configurations.

These tunneling systems are ubiquitous and form an ensemble of TLS defects, whose low-energy excitations account for the observed linear temperature dependence of the specific heat capacity. Early models treated TLS defects as non-interacting and uniformly distributed in

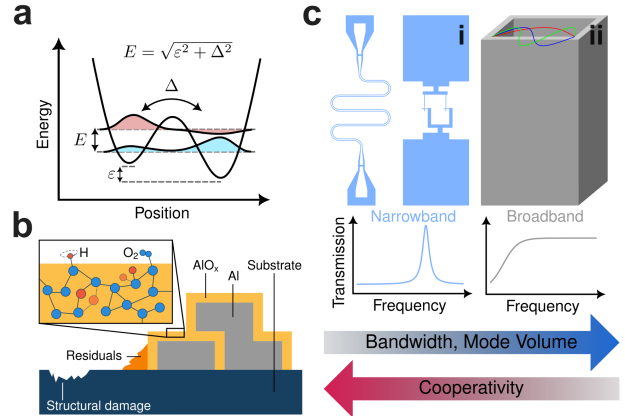


Figure 1. Overview of TLS defects and how they can be probed. **a**, Double-well representation of TLS defects described by the standard tunneling model. **b**, Candidate TLS defects and their potential locations in superconducting circuits. **c**, Comparison of traditional TLS defect spectroscopy using 2D qubits and resonators and our proposed broadband 3D waveguide approach. Image in **a** is adapted from [4].

frequency, which sufficed to explain the specific heat measurements. However, studies have shown that TLS defects can interact, leading to spectral diffusion, clustering, and nonlinear loss [5–11].

While the notion of a TLS defect was initially developed to explain the thermodynamic properties of glassy

* mattias.w.fitzpatrick@dartmouth.edu

materials, such defects have recently regained relevance in solid-state quantum computing technologies. This renewed interest is especially evident in superconducting circuits, which have become a leading platform primarily due to their fast gate times, design flexibility, and compatibility with advanced semiconductor fabrication techniques. However, their decoherence times are relatively short compared to other promising quantum technologies, such as neutral atoms, trapped ions, or spin qubits. From measurements of bulk loss tangents [12, 13], and modeling of the Purcell effect [14–16], it became clear that other sources of loss must be present. Pioneering studies examining the impact of electric fields and mechanical strain on qubit coherence provided explicit evidence of TLS defects in superconducting circuits [17–21]. Today, it is widely believed that TLS defects are the dominant source of decoherence of superconducting circuits and that they likely reside at surfaces and interfaces [22–26] (Fig. 1b) with no clear consensus as to their specific atomistic origin.

TLS defects are typically probed via photonic or acoustic resonators [27–31] and qubits [12, 17–20, 32]. These approaches provide high cooperativity but preferentially detect TLS defects with dipole moments aligned with the directly integrated probes, and are restricted to small bandwidths and mode volumes (Fig. 1c). Despite this limitation, several studies have demonstrated the existence of TLS-TLS interactions [19, 33, 34], and non-Markovian dynamics [35, 36], leading to questions about the nature of TLS-TLS interactions in the absence of strongly coupled probes [37].

In addition to their impact on the decoherence of superconducting qubits, TLS defects also influence the fidelity of qubit readout. In particular, TLS defects can manifest in Josephson traveling wave parametric amplifiers (JTWPs), which are crucial for high-fidelity qubit readout due to their quantum-limited amplification and several GHz of bandwidth [38]. However, recent experiments show that high-power pulses can excite long-lived dielectric echoes in JTWPs, which are attributed to TLS defect ensembles [39, 40]. These echoes impair the readout fidelity of experiments utilizing JTWPs (and likely other parametric amplifiers), motivating careful characterization of the transient dynamics of interacting TLS defect ensembles.

Here, we propose a novel, modular, noninvasive technique that enables broadband dielectric spectroscopy of TLS defect ensembles in isolated materials and material stacks. Through systematic, longitudinal studies, this technique will provide essential data that will shed light on the atomistic nature of TLS defects and their properties [41]. Such insights will inform the design of the next generation of quantum hardware from a first-principles understanding of TLS defects, something which was recently highlighted as a pressing need for the superconducting qubit community by the Google Quantum AI Hardware team [42].

II. CRYOGENIC DIELECTRIC SPECTROSCOPY

Modular, Broadband 3D Microwave Waveguide

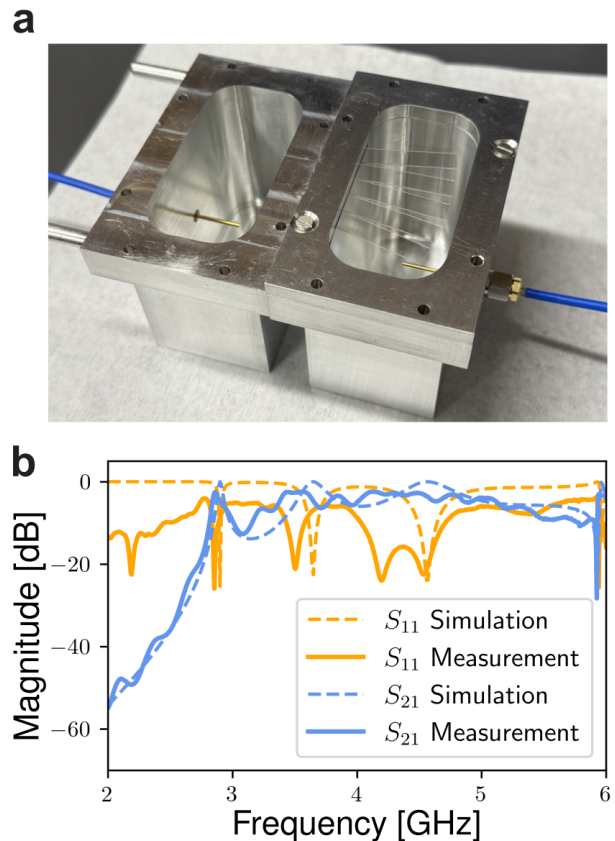


Figure 2. Broadband waveguide design. **a**, Photograph of upper and lower WR-229 to SMA adapter components and clamp with sapphire samples. These components are assembled to create the closed 3D aluminum waveguide used in this work. **b**, HFSS simulated and measured transmission (S_{21}) and reflection (S_{11}) spectra of the waveguide containing samples at room temperature, demonstrating a waveguide cutoff of 2.8 GHz and broadband transmission from 2.8–6 GHz.

To probe the dielectric response in the microwave frequency domain, we leverage a broadband 3D waveguide (Fig. 2a). In contrast to qubit and resonator-based probes, this method allows coupling to ensembles of TLS defects over a broad frequency range (Fig. 1c). As described in Appendix A, the closed waveguide comprises two WR-229 to coaxial cable adapters joined by a sample clamp. This modular approach allows us to easily measure samples of various sizes, shapes, and material compositions (Fig. 2b). Importantly, these features distinguish our approach from existing narrow-band qubit and resonator-based probes, which require samples to go through a full fabrication cycle, followed by wire bonding and packaging, making it challenging to perform additional material processing and characterization.

Dielectric Response of an Ensemble of TLS Defects

Applying an external electric field to dielectric materials induces a time-dependent polarization that reflects the collective dielectric response. This response is dominated by a distribution of atomic-scale TLS defects at low temperatures, whose energy splittings and coupling strengths vary widely due to structural disorder. Within the linear response regime, the relationship between the applied field and the induced polarization is captured by the dynamical susceptibility of the material, which encodes both in- and out-of-phase components of the TLS ensemble response. In our experiment, the response can extend beyond the linear region when the system is influenced by strong, broadband, or pulsed electric fields, making the susceptibility dependent on amplitude, leading to higher-order contributions. In this context, we use the dynamical susceptibility framework as a conceptual tool to interpret the response, even though saturation and non-linear effects play an essential role. After the drive is turned off, the system enters a transient regime, where the energy absorbed by TLS defects begins to dissipate. By monitoring the subsequent time evolution of the polarization using homodyne detection, we perform broadband transient dielectric spectroscopy, which reveals signatures of the TLS defects dynamics.

We consider a single TLS defect characterized by an energy detuning ε_j and a tunneling amplitude Δ_j , as illustrated in Fig. 1a. The effective Hamiltonian for the j -th TLS defect in the position basis $\{|L\rangle, |R\rangle\}$ can be written as [19]

$$\hat{H}_j = \frac{1}{2} \begin{pmatrix} \varepsilon_j & \Delta_j \\ \Delta_j & -\varepsilon_j \end{pmatrix} = \frac{1}{2} \varepsilon_j \hat{\sigma}_z^{(p,j)} + \frac{1}{2} \Delta_j \hat{\sigma}_x^{(p,j)}, \quad (1)$$

where $\hat{\sigma}_z^{(p,j)}$ and $\hat{\sigma}_x^{(p,j)}$ are Pauli matrices in the position basis representing the difference between left and right localized states.

Diagonalizing this Hamiltonian yields the energy eigenstates with eigenenergies

$$E_j = \sqrt{\varepsilon_j^2 + \Delta_j^2}, \quad (2)$$

and defines a mixing angle θ_j through

$$\tan \theta_j = \frac{\Delta_j}{\varepsilon_j}. \quad (3)$$

Transforming to this energy eigenbasis, the static Hamiltonian simplifies to

$$\hat{H}_{0,j} = \frac{1}{2} E_j \hat{\sigma}_z^{(j)}, \quad (4)$$

where $\hat{\sigma}_z^{(j)}$ now acts in the energy eigenbasis.

Next, we introduce the interaction of the TLS defect ensemble with an external, time-dependent electric field $\mathbf{E}(t)$. The coupling occurs via the electric dipole moment

\mathbf{p}_j of the TLS defect. Choosing the dipole moment direction as the quantization axis (here aligned along $\hat{\mathbf{x}}$), the collective polarization operator for an ensemble of N TLS defects can be defined as

$$\hat{\mathbf{P}} = \sum_{j=1}^N p_j \left(\cos \theta_j \hat{\sigma}_z^{(j)} + \sin \theta_j \hat{\sigma}_x^{(j)} \right) \hat{\mathbf{x}}, \quad (5)$$

where the Pauli operators are in the energy eigenbasis.

The full Hamiltonian, including the interaction with the electric field, is then written as

$$\hat{H}(t) = \sum_{j=1}^N \hat{H}_{0,j} - \hat{\mathbf{P}} \cdot \mathbf{E}(t). \quad (6)$$

In typical experimental setups, the electromagnetic field is polarized and can be represented as

$$\mathbf{E}(t) = (E_0 e^{-i\omega_0 t} + E_0^* e^{i\omega_0 t}) \hat{\mathbf{x}}, \quad (7)$$

where E_0 is the complex amplitude and ω_0 the driving frequency.

This formulation captures the static energy structure of the TLS defect ensemble and its collective coupling to the external, oscillating electric field. However, in practice, the dynamical response includes additional features such as dynamical Stark shifts and nonlinearities [43]. In previous narrow-band probe experiments using qubits and resonators, the driving is typically focused on the qubit or resonator, and such direct driving of TLS defects is ignored. The driving term in Eq. 6 is absent in the standard tunneling model.

The interaction in Eq. 6 causes an induced dipole moment with expectation value $\langle \hat{P}(t) \rangle$. Assuming that the medium is isotropic and the polarization is parallel to the electric field, we can express the average polarization using the Kubo formula [44]

$$\langle \hat{P}(t) \rangle = \int_{-\infty}^{\infty} dt' \chi(t-t') E(t'), \quad (8)$$

where E is the amplitude of the electric field, and the susceptibility is given by

$$\chi(t) = i\theta(t) \langle [\hat{P}(t), \hat{P}(0)] \rangle_0, \quad (9)$$

where $\langle \dots \rangle_0$ denotes the equilibrium expectation value and $\theta(t)$ is the Heaviside step function. Note that the Kubo framework introduced here is only a conceptual tool to motivate the spectroscopic technique. The observed transient response in our experiment seems to suggest nonlinear contributions to the susceptibility, and we are likely far from the linear regime. However, we can still proceed by considering the Fourier transform of the induced polarization, which is given by

$$\langle \hat{P}(\omega) \rangle = \chi(\omega) E(\omega), \quad (10)$$

where

$$\chi(\omega) = \int_{-\infty}^{\infty} dt e^{i\omega t} \chi(t). \quad (11)$$

Here we will be primarily concerned with the loss induced by such an interaction, which is given by the imaginary component of Eq. 11

$$\chi''(\omega) \equiv \text{Im } \chi(\omega) \quad (12)$$

When the electromagnetic field is on, the loss described by Eq. 12 causes a decrease in the measured transmitted signal. However, when this drive is turned off and we enter the transient regime, the energy absorbed from the drive must now be dissipated. Given the insulating nature of the sapphire sample and the superconducting waveguide, a portion of the absorbed energy will be re-emitted and ultimately measured from the output signal of the waveguide. Thus, transient dielectric spectroscopy gives us a direct measure of $\chi''(\omega)$ without an input drive. To extract the radiated field to learn about $\chi''(\omega)$, we perform homodyne detection, which involves extracting the classical output field quadratures $I(t)$ and $Q(t)$ and computing the amplitude $A(t) = \sqrt{I^2(t) + Q^2(t)}$. By input-output theory [45], the output field is proportional to the dipole response,

$$A(t) \propto \langle \hat{P}(t) \rangle e^{i\omega_0 t}. \quad (13)$$

Thus, following Novotny et al. [46], we can express the imaginary part of susceptibility using the experimentally obtained intensity $\mathcal{I}(t) \propto A^2(t)$ as

$$\chi''(\omega) \propto \text{Im} \int_{-\infty}^{\infty} dt e^{i\omega t} \langle \mathcal{I}(t) \mathcal{I}(0) \rangle. \quad (14)$$

Cryogenic Transient Dielectric Spectroscopy

In principle, transient dielectric spectroscopy can be performed on any dielectric sample at any temperature. Furthermore, even metallic or superconducting samples with oxide layers can be probed in reflection. Here, we will be primarily interested in the dielectric response of TLS defects, which solely arise at cryogenic temperatures, as described in Sec. I. Therefore, to extract information about the TLS defects, we perform cryogenic dielectric spectroscopy on our samples by inserting them into the waveguide (Fig. 2a) and cooling it to 10 mK using a dilution refrigerator. As electromagnetic waves propagate through the waveguide and interact with the samples, they polarize the electric dipoles of the TLS defects, revealing their intrinsic dielectric response. This work considers cryogenic dielectric spectroscopy in both driven and transient regimes: driven dielectric spectroscopy monitors the response during the pulse, while transient dielectric spectroscopy monitors the post-pulse region (also known as the ring-down).

To probe a driven dielectric response, we generate 30-ns square pulses in the 3-5 GHz band, similar to those employed for superconducting-qubit gate operations. The simple square pulses we explore here are synthesized directly on an FPGA (Field Programmable Gate Array) board (AMD RFSoC 4x2) using the Quantum Instrumentation Control Kit (QICK) software package [47]. We send the pulses through a room-temperature amplifier (Minicircuits CMA-83LN+) and into a dilution refrigerator (Bluefors LD400) where they are attenuated and ultimately reach the 3D waveguide, exciting the sample (See setup diagram in Appendix E). The resultant signal is amplified using cryogenic high-electron-mobility transistor amplifiers from Low Noise Factory before being measured on the RFSoC.

Following the cessation of the external drive, the induced polarization in the medium relaxes, leading to a coherent emission in the transient dielectric response, which imprints the temporal decay of the TLS defect ensemble on the outgoing field. A strong time-dependent drive may also modify the phonon-induced decay rate of a TLS by hybridizing its states (dressed states), thereby shifting transition frequencies and enabling decay through induced sidebands. This may alter the coupling to the spectral density of the phonon bath, leading to either enhanced or suppressed relaxation depending on the drive strength. Although we do not investigate this effect here, the broadband nature of our technique should enable its detailed study in future experiments.

III. RESULTS

Cryogenic Dielectric Spectroscopy of Different Materials

As described in Sec. II, our waveguide enables a modular characterization of the driven and transient dielectric response of TLS defect ensembles in various samples. The samples considered in this study started with a 50.8 mm diameter, 432 μm thick, wafer of ultra-high-purity HEMEX sapphire from Crystal Systems, which has been measured to have bulk loss tangents of the order 10^{-7} [13]. We spin coat the samples with photoresist and dice them into rectangular chips with 27.5×5.5 mm dimensions. We clean the samples with solvents following a standard procedure described in Appendix B and mount them in the waveguide (Fig. 2a), which is cooled to 10 mK in a dilution refrigerator.

Figure 3 summarizes the dielectric spectroscopy results obtained for different materials, alongside a room temperature control experiment of bare sapphire samples that serves as a benchmark. Given that the TLS defects observed in our experiments have frequencies between 3 and 5 GHz, small temperature changes can significantly impact their thermal occupation, a key signature that has been explored in previous work [48, 49]. Furthermore, increases in temperature cause thermal oc-

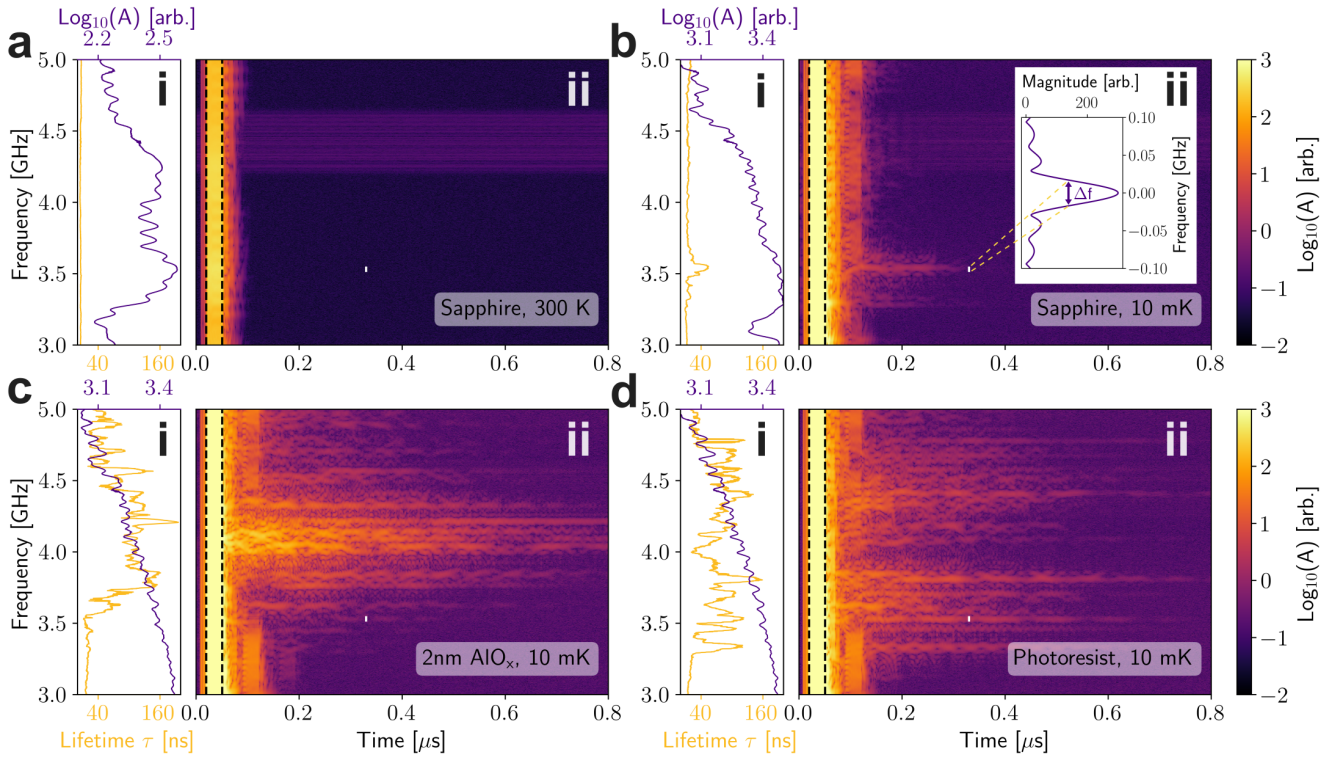


Figure 3. Dielectric spectroscopy of different samples. We perform dielectric spectroscopy using a 30 ns pulse (marked by vertical black dashed lines) followed by a long readout with a total measurement time of 0.8 μ s. **a**, Control experiment at room temperature with solvent-cleaned sapphire samples, showing no detectable transient dielectric response. The horizontal band around 4.4 GHz is due to readout electronics, which exhibit a slightly higher noise floor in that frequency range. **b**, Same setup as in **a**, measured at 10 mK (as with **c-d**), revealing coherent transient dielectric response features arising from TLS defects. **c**, The same samples as **b** with a 2 nm aluminum oxide layer deposited via atomic layer deposition (ALD). **d**, The same samples as **b** with spin-coated Shipley 1813 photoresist. Transient dielectric response in **c-d** shows prominent features in the ring-down, which we attribute to increased TLS defect density. Subpanels **i** show the average driven dielectric response and the extracted lifetimes (τ) of the transient dielectric response, which is fitted from the ring-downs, considering a simple exponential function. Regions with large τ exhibit dips in the driven dielectric response, as expected. Subpanels **ii** show the driven and transient dielectric response for various samples with the color scale clipped to reveal weaker transient features. In **b,ii**, we include a vertical white line to indicate the full width at half-maximum of the pulse, Δf , whose FFT is shown explicitly in the inset and has approximately the same bandwidth as the prominent spectral features in the transient dielectric response. Note that the electric field at the sample plane is frequency dependent and can be calibrated by reducing signal amplitude at certain frequency ranges, as described in Appendix D. For the results displayed in this work, we apply an even amplitude drive across the span to capture maximum response.

cipation of phonon modes, which can cause incoherent shaking of the double-well potential of the TLS defects, likely broadening or destroying any spectral features. As motivated in Sec. II, linear response theory suggests that the spectral dips of the driven dielectric response should be corroborated by the longer-lived coherence times in the transient region, which is saturated at room temperature (Fig. 3a, ii).

In contrast, when the same sample in Fig. 3a is cooled down to 10 mK, we see an apparent narrowing of the spectral dips in the driven dielectric spectroscopy (Fig. 3b,i) and a corresponding increase in the coherence of the transient dielectric response (Fig. 3b,ii). Appendix C provides a more detailed demonstration of this effect (using the sample in Fig. 3c) by zooming into a nar-

rower frequency range and varying the pulse lengths. Most emission locations align with the absorption minima during the drive. As the pulse length increases, the absorption features deepen, and the associated emission peaks exhibit increased sharpness, providing clear signatures of coherent energy storage and re-emission by the TLS defect ensemble. In Fig. 3 b, we conjecture that these defects arise from residual surface contamination due to leftover photoresist, adventitious carbon, surface damage, dicing damage, or the waveguide and antenna surfaces. In future work, we intend to explore further surface treatments such as etching, annealing, and passivation to reduce the measured transient dielectric response of bare sapphire and silicon wafers [50–52].

Today, most Josephson junctions are fabricated using

various versions of double-angle evaporation, where the insulating Josephson junction layer is formed from a native oxide grown on deposited aluminum. However, all regions of the chips that contain aluminum will inadvertently grow such native oxides, and therefore, most superconducting circuits inevitably contain large areas of aluminum oxide. To emulate the native oxide in Josephson junctions and aluminum metal layers, we grow a thin, 2 nm aluminum oxide layer in an atomic layer deposition tool on a bare sapphire wafer, like those measured in Fig. 3a-b (see Appendix B). The results of these dielectric spectroscopy measurements are shown in Fig. 3c. Here, we see obvious signatures of TLS defect ensembles, primarily in the transient region. The transient response exhibits pronounced collapse and revivals due to the interplay between external driving and TLS-defect ensemble interactions, clearly indicating memory effects in the environment [20, 53]. Furthermore, we want to highlight that the deposited 2 nm of aluminum oxide is approximately 5×10^{-6} times the volume of the substrate, but is composed of the same atomic species. These findings demonstrate the importance of material morphology in the existence and behavior of TLS defects and motivates future work on passivating metallic layers [54] and developing crystalline insulating layers for Josephson junctions. This work also suggests why tantalum, which hosts a thin, stoichiometric native oxide, is an advantageous material choice for high-coherence superconducting circuits [26, 50].

Finally, we also characterize the dielectric response of 1-4 μm of photoresist on sapphire, as shown in Fig. 3d. This investigation is especially relevant because most resonators and waveguides leverage photolithography, meaning residual photoresist may be left on substrates if improperly removed. These photoresists are complex polymer chains that likely contain a high density of TLS defects [4, 55] (a detailed description of sample preparation is included in Appendix B). By understanding the dielectric properties of the resist layer, we can better assess its impact on junction performance and guide fabrication and device design optimizations [42]. Therefore, in Fig. 3d, we observe more transient response, consistent with our hypothesis that photoresist has many TLS defects.

The technique presented in this manuscript also enables future longitudinal studies where the sample can be characterized at each step of the fabrication process, and it envisions active mitigation strategies for these defects in the next generation of superconducting qubit devices. It is essential to highlight that in the data presented in Fig. 3, we observe that the transient emission processes have lifetimes on the order of 100 ns. Previous work on so-called dielectric echoes in JTWPA experiments [39, 40] measured lifetimes of $\approx 1 \mu\text{s}$. Here, since the waveguide provides a large density of states and probes large ensembles, the lifetimes of these TLS defects may be reduced due to Purcell enhancement and stimulated emission. While the lifetimes extracted in these

measurements are relatively short compared to state-of-the-art coherence times for superconducting qubits, the observed transient response can still play a prominent role in larger quantum circuits where gates are sequentially implemented. This effect may partially explain why large quantum circuits have overall fidelities lower than a naive calculation based on single and two-qubit gate fidelities extracted using randomized benchmarking [56].

Cryogenic Dielectric Spectroscopy of the Same Sample, For Different Cooldowns

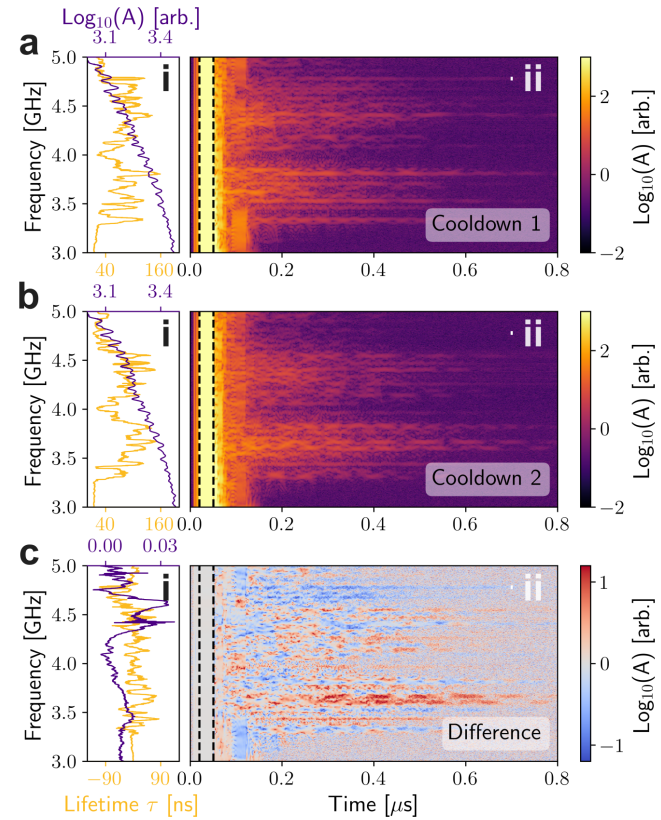


Figure 4. Cryogenic dielectric spectroscopy measurements of Shipley 1813 photoresist on sapphire over different cooldowns. **a**, Cooldown 1 (the same data as Fig. 3d). **b**, Cooldown 2, with the same sample as **a**, but after warming up to 300 K. **c**, Difference in dielectric response between cooldowns 1 and 2, demonstrating completely distinct spectral fingerprints. Note that the datasets in **a** and **b** were acquired 15 days apart, meaning that some of the change in the dielectric response could be due to subtle drifts of the TLS defects at cryogenic temperatures, which are known to happen. However, the predominant changes are likely morphological, primarily from thermal cycling. A short vertical white line is added to indicate pulse bandwidth Δf , similar to Fig. 3b.

Much like point defects in crystals, which spatially migrate at high temperatures, it is well-understood that thermal cycling of TLS defects, even up to a few K, can

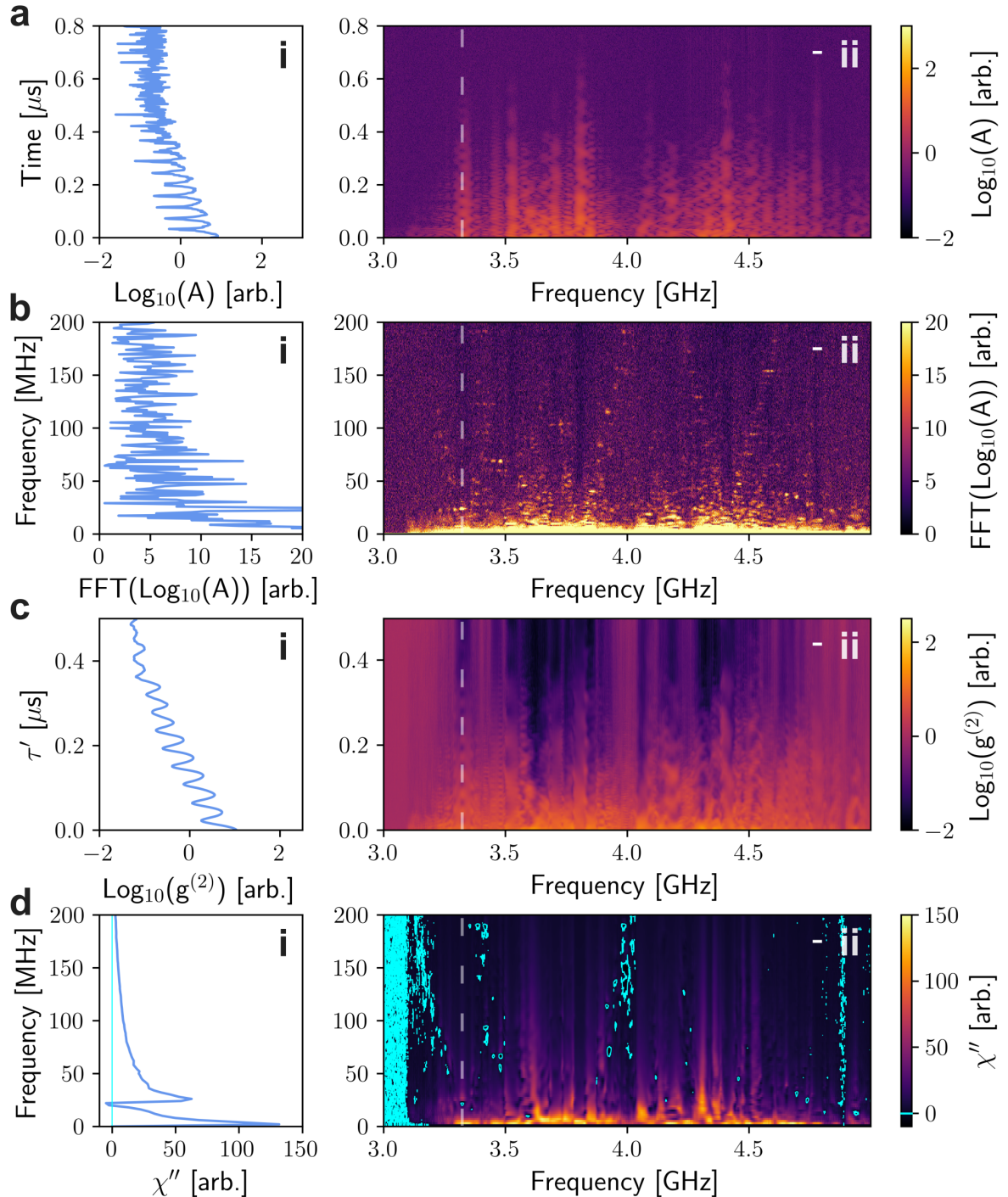


Figure 5. Transient dielectric response of Shipley 1813 photoresist on sapphire, same data as Fig. 3d. **a-ii**, Logarithmic magnitude of the transient dielectric response. **b-ii**, Magnitude of Fast Fourier transform (FFT) of the logarithmic amplitude. **c**, Log of the two-time correlation function $g^{(2)}$ map of the transient spectrum, defined by equation 15. **d-ii**, χ'' computed from $g^{(2)}$ using equation 14. We highlight transitions from positive to negative χ'' with the cyan contour in **d-ii**. **a-d,i** show linecuts at $\omega/2\pi = 3.322$ GHz (dashed line in **ii**), highlighting distinct memory effects in the form of collapse and revivals in the ringdown (**a**), sharp spectral features in the FFT (**b**), non-exponential decay, bunching, and oscillations indicative of non-Markovian dynamics (**c**), non-monotonic and negative χ'' (**d**). The negative regions are consistent with the bright FFT features in (**b**). It should be noted that χ'' oscillates around zero near $\omega/2\pi = 3$ GHz primarily due to weak signals and not necessarily indicating memory effects. A short horizontal white line is added to indicate pulse bandwidth Δf .

cause them to move considerably in frequency and potentially in physical location. To corroborate this signature of TLS defects, we perform dielectric spectroscopy experiments 15 days apart on the same sample subject to a thermal cycle to 300 K in Fig. 4. As expected, we see a significantly different driven and transient dielectric response in Fig. 4a-b, highlighted by the difference plot in Fig. 4c. In future work, we intend to perform systematic studies of the temperature dependence closer to 10 mK to observe the thermal occupation and ultimate dissolutions of TLS defects. Such studies may provide insights into the observed ‘universal’ dielectric response, and potentially probe the transition of quantum TLS defects to the broad classical dielectric response [57, 58].

Further Investigation of Cryogenic Transient Dielectric Spectroscopy Results

In this section, we provide a more in-depth analysis of the transient dielectric response from the sample in Fig. 3d containing photoresist on sapphire, which is shown in Fig. 5. We start by plotting the transient dielectric response in Fig. 5a,ii showing long-timescale oscillatory collapse and revival behavior of the emitted signal, which indicates information backflow and memory effects [59, 60]. This can be seen clearly in Fig. 5a,i, which displays the response at a single frequency of $\omega/2\pi = 3.322$ GHz. To quantify the frequency components of the oscillations observed in the time traces in Fig. 5a, we perform Fast Fourier Transforms (FFT) of all the data traces to generate Fig. 5.b,ii. Again, a particular line cut at the same frequency is shown in Fig. 5b,i. The FFT clearly shows the emergence of distinct V-shaped frequency components and horizontal bands across parts of the FFT spectrum (e.g. at frequency range 3.65-4.0 GHz, and 4.25-4.65 GHz). These V-shapes can be attributed to the off-resonant emission of the dominant eigenfrequencies of the TLS defect ensembles, which are prominent due to the broadband nature of the waveguide [61].

We also compute the two-time correlation function $g^2(\tau')$ [62]

$$g^{(2)}(\tau') = \frac{\langle \mathcal{I}(t)\mathcal{I}(t+\tau') \rangle}{\langle \mathcal{I}(t) \rangle^2}, \quad (15)$$

where $\mathcal{I}(t) \propto A^2(t)$ is the intensity of the transmitted pulse, and plot it in Fig. 5c. $g^{(2)}(\tau')$ provides us with a map of temporal correlations and displays evident non-exponential, oscillatory decay, which is a hallmark signature of memory effects and non-Markovian dynamics of the TLS defect ensemble. Finally, we utilize the computed $g^{(2)}(\tau')$ to extract $\chi''(\omega)$ using Eq. 14, which we show in Fig. 5d. Here, consistent with the $g^{(2)}(\tau')$, we observed the non-monotonic and negative $\chi''(\omega)$, accentuated by the cyan contours in Fig. 5d, further supporting the claim of memory effects and re-emission in the TLS defect ensemble. The cyan contour highlights the

negative areas of $\chi''(\omega)$, which indicate physics beyond linear response, exhibiting partial overlap with the aforementioned V-shapes in some regions of the FFT [63, 64].

IV. CONCLUSIONS AND OUTLOOK

This work introduces cryogenic transient dielectric spectroscopy, a novel technique to probe TLS defects that supports fast, modular mounting of various samples. Our measured cryogenic dielectric spectroscopy experiments reveal distinct transient features and memory effects as demonstrated by the $g^{(2)}$ and χ'' plots in Fig. 5c,d, respectively. Such memory effects may indicate that the dynamics are non-Markovian, which could create problems for quantum error correction if manifested in quantum processors [53, 65, 66]. We believe that much of the memory effects arise from the interplay between coherent TLS defects and driving in a broadband environment. By analyzing the spatial and temporal correlations of large TLS defect ensembles in isolated materials, we take initial steps toward uncovering the atomistic structure of TLS defects. Next, we aim to introduce an orthogonal SMA port to rotate the polarization of the drive and perform the same dielectric spectroscopy experiments, subject to different drive strengths. By integrating over different drive polarizations, we can better understand the frequency distribution and dipole moments of the TLS defects in various samples.

While this work has focused on materials for superconducting qubits, we highlight that cryogenic transient dielectric spectroscopy is a more general technique that provides information about the atomistic structure of various dielectric materials. The response is also not exclusively driven by TLS defects, and we may be able to measure point defects as well. For instance, transient dielectric spectroscopy of silicon (diamond) samples may allow us to measure silicon (nitrogen) vacancies without needing optical interrogation. In conclusion, we have demonstrated a novel spectroscopy tool based on a broadband 3D waveguide that enables global interrogation of TLS defect ensembles. The approach is entirely modular, and we demonstrate that this can be leveraged for longitudinal devices that can help develop causal relationships between TLS defect ensemble properties and material processing steps.

DATA AVAILABILITY STATEMENT

The data that support the findings of this study are available from the corresponding author upon reasonable request.

Appendix A: Waveguide Design and Fabrication

1. Waveguide Design

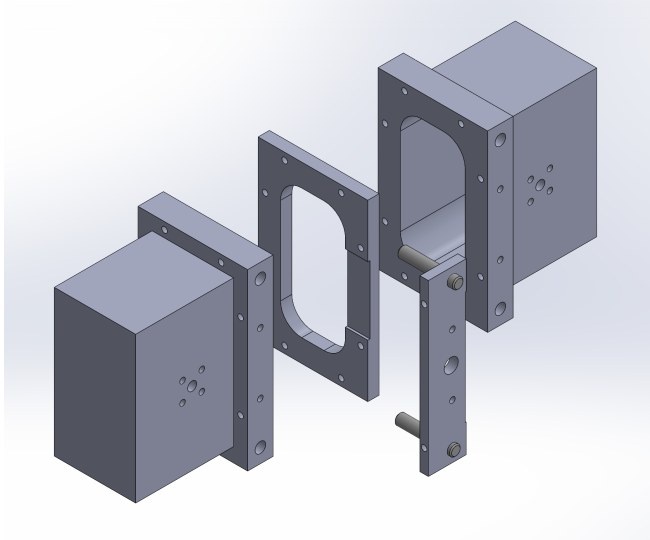


Figure 6. Exploded view of waveguide assembly.

The fundamental building block of our waveguides is an adapter that provides a 50Ω impedance-matched conversion between an SMA coaxial cable and a WR-229 3D rectangular waveguide. To understand the basic features of the waveguide, we solve the wave equation for a rectangular prism, with boundary conditions that the electric field goes to zero at the walls of the waveguide. After performing separation of variables, we can identify a set of allowed eigenmodes for the cross section perpendicular to the direction of propagation, with wavenumbers given by

$$k_c = \sqrt{\left(\frac{m\pi}{a}\right)^2 + \left(\frac{n\pi}{b}\right)^2}, \quad (\text{A1})$$

where a and b are the width and height of the rectangular cross-section of the waveguide, respectively. The constants m and n are integers whose combinations identify different eigenmodes of the cross-section. This means that the propagation constant of the transmitted wave can be expressed as

$$\beta = \sqrt{k^2 - k_c^2}, \quad (\text{A2})$$

where k is the wavenumber. Significantly, Eq. A2 predicts that when $k^2 < k_c^2$, β becomes imaginary, and the solutions become decaying exponentials along the waveguide in a domain known as the waveguide's cutoff [14]. Therefore, we can describe the frequencies of the allowed modes of the waveguide using

$$f_{c_{mn}} = \frac{k_c c}{2\pi}, \quad (\text{A3})$$

where c is the speed of light. From Eq. A3, we then identify the cutoff frequency, which is the lowest frequency TE_{10} mode, given by

$$f_{c_{10}} = \frac{c}{2a}, \quad (\text{A4})$$

assuming that $a \leq b$. The cutoff frequency formula provided in Eq. A4 is idealized and assumes a perfect rectangular waveguide, which is challenging to manufacture in practice due to the sharp inner corners. Therefore, we utilize Ansys HFSS to consider the design of the actual waveguide in this work. The drive and readout ports are coaxial SMA cables that transition into small antennas integrated into the waveguide. This coupling scheme smoothly transforms the coaxial mode of the SMA cables to a close approximation the TE_{10} mode of an ideal rectangular waveguide, producing a polarized electric field that will ultimately couple to the TLS defects in the sample.

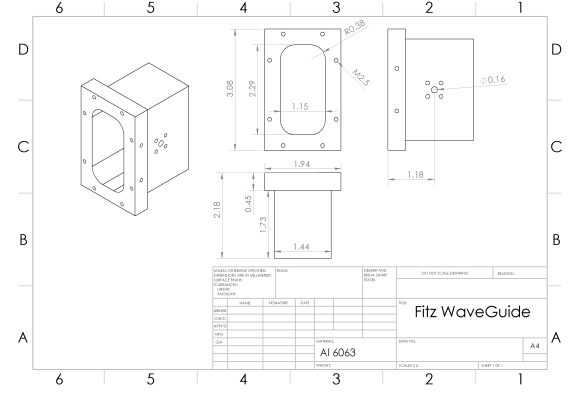


Figure 7. Designs for SMA to WR-229 3D rectangular waveguide adapter utilized to build the 3D waveguide.

Figure 7 provides detailed dimensions of our SMA to WR-229 3D rectangular waveguide adapter. In this work, we leverage Eq. A4 to achieve the desired 2.8 to 6 GHz frequency band and adapt the perfect rectangular waveguide designs to make the manufacturing easier. In particular, our design features an inner radius of the 3D waveguide designed to use a 3/8 inch end mill. M2.5 screws are used to mount the 4.1 mm SMA pins that integrate into the designs shown in Fig. 7.

We fabricate two copies of the SMA to WR-229 3D rectangular waveguide adapter to construct a full waveguide. Then, we construct a clamp for samples that can be introduced between the two waveguide adapters. This approach allows us to consider a variety of sample layouts and sizes. The assembly of the complete waveguide can be seen in Fig. 6.

2. Waveguide Fabrication

The waveguide used in this manuscript is manufactured from Aluminum 6061 using a HAAS Super Mini

Mill in Dartmouth's Thayer School of Engineering machine shop. A combination of steel wire wool and polishing stones was used to improve the surface finish, especially the rounded corners, and remove any feed marks left behind from the end mill. Finally, the waveguide was cleaned using isopropanol (IPA) to remove impurities and oily residues.

Appendix B: Sample Processing

To demonstrate the modularity of our platform, we consider three types of samples, the preparation of which is explained in this section.

We start with high-grade crystalline 0.5 mm-thick sapphire wafers from Crystal Systems, which are then diced into 27.5 x 5.5 mm rectangular strips, the standard substrate size for hosting 3D transmons. The samples are initially covered in resist AZ 1518 to protect them from debris during dicing (likely another source of TLS defects). We soak the chips in acetone at 70 °C overnight and sonicate them in acetone before transferring them to IPA and drying with compressed air.

To study the effects of photoresist on the TLS density, we spin-coat Shipley 1813 with thicknesses ranging from 1 to 4 μm . We also study the oxide layers (typically a few nanometers in thickness), another candidate source of TLS defects. Instead of evaporated aluminum, which would give both an aluminum and oxide layer, we used an atomic layer deposition (ALD) machine to grow a 2 nm thin film. We expect the entire film to be oxidized by doing 20 burst cycles at 80 °C and repeatedly using H_2O as an oxidant at each burst.

Appendix C: Dielectric Response under Different Drive Lengths

We examine the driven and transient dielectric response under drive pulses of varying lengths in Fig. 8, featuring 20 ns (a), 50 ns (b), and 200 ns (c) pulses. To clearly display subtle features, we restrict the analysis to a narrower frequency window of 3.9-4.4 GHz.

Increasing the drive length improves spectral resolution and strengthens on-resonance driving on TLS defects. This manifests as sharper and deeper absorption dips during the pulse, due to increased spectral selectivity as the drive couples more effectively to resonant TLS defects. After the drive is turned off, a similar effect is seen in the transient emission, where we observe increased sharpness and prolonged lifetimes in correspondence to the reduced bandwidth of the drive. This result is consistent with both our conceptual model and numerical simulations (to be presented elsewhere). Moreover, even without controlled access to physical parameters of the TLS defects, it is encouraging to observe changes in TLS dynamics as a result of different pulses. These

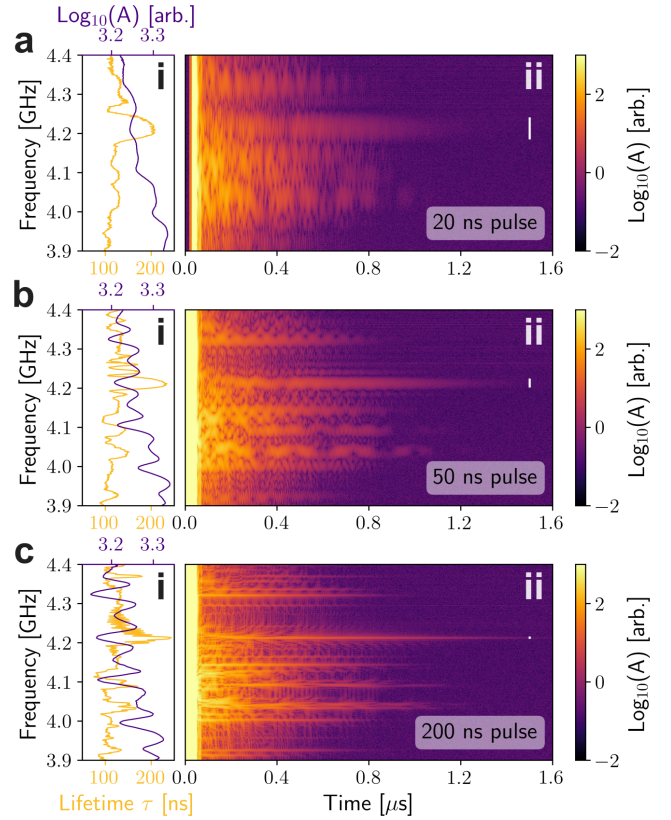


Figure 8. Dielectric response of 2nm aluminum oxide under different pulse lengths. **a**, 20 ns pulse. **b**, 50 ns pulse. **c**, 200 ns pulse. As the pulse length increases, the bandwidth (marked by the short vertical white lines) of the pulse decreases, resulting in sharper emissions. Absorption in the pulsing region often corresponds to an emission around the same frequency, after the pulse is turned off.

findings support the feasibility of pulse-based coherent control of TLS defect ensembles.

Appendix D: Electric Field Amplitude Calibration

The waveguide design ensures that the transmitted signal is relatively constant over a bandwidth of approximately 2.8-6 GHz (Fig. 2b). However, the samples under test are coupled in the middle of the waveguide, which can be frequency-dependent as illustrated in Fig. 9. We leverage HFSS simulations to predict the electric field amplitude at the sample plane over our frequency bandwidth (blue dot and lines in Fig. 9b). To compensate for this variation, we apply a frequency-dependent scaling factor (red solid line in Fig. 9b). The impact of this calibration is evident when comparing the transient spectra of a photoresist-coated sapphire sample before (Fig. 9c) and after applying the correction (Fig. 9d). Significantly, most of the key features in the data remain. Still, such calibrations can ensure uniform electric field den-

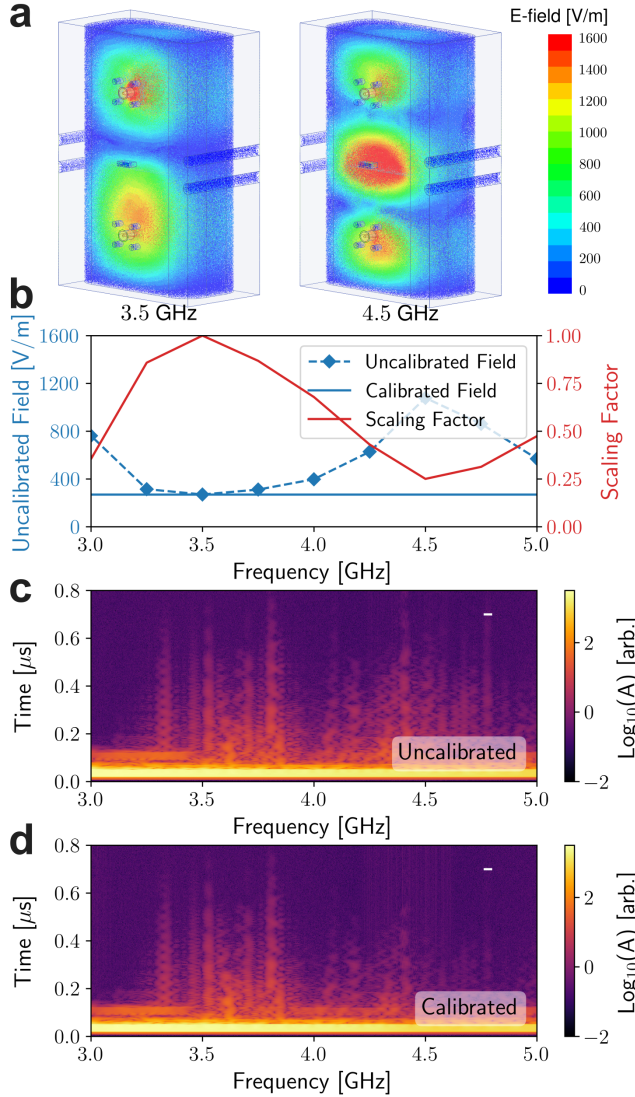


Figure 9. Electric field amplitude calibration at the sample plane. **a**, HFSS simulation of the electric field distribution in the waveguide at 3 GHz and 5 GHz. The simulation applies an input power of 1 W at the SMA port to excite the dominant mode. The snapshot is taken for both frequencies when the oscillating electric field reaches its maximum amplitude at the sample plane. **b**, Frequency-dependent electric field strength averaged over the sample plane and time (blue solid line). A scaling factor is applied to the pulse (red solid line) to achieve a uniform drive amplitude across the band, reducing the amplitude in regions with higher intrinsic field strength. The resulting average field profile is flattened (blue dashed line). **c,d**, Comparison of transient spectra for a photoresist-coated sapphire sample before (**c**) and after (**d**) field calibration. The calibrated spectrum shows reduced amplitude in previously over-driven regions and yields a more uniform interrogation of the TLS ensemble across the full spectral range. A short horizontal white line is added to indicate pulse bandwidth Δf .

sities as a function of frequency and may prove critical in future experiments to deduce properties of individual TLS defect ensembles.

Appendix E: Measurement Setup

This work utilizes an AMD radio-frequency system on a chip (RFSoc) board, which provides a fast sampling rate (9.85 GSPS for DAC and 5 GSPS for ADC) and direct synthesis and readout of microwave pulses without needing up- and down-conversion. To control the RFSoc, we utilize the Quantum Instrumentation Control Kit, a Python package developed by Fermi National Accelerator Laboratory [67].

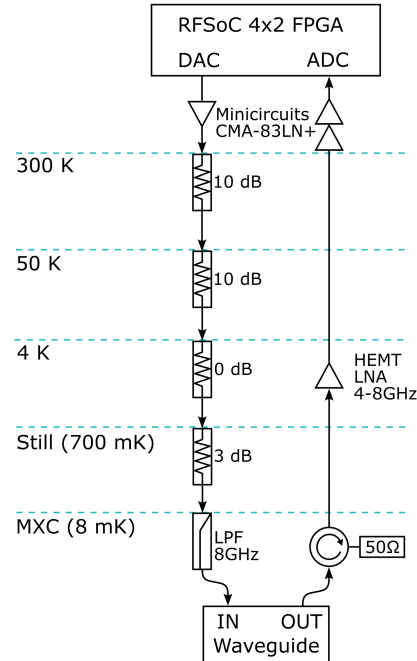


Figure 10. Measurement setup for transient dielectric spectroscopy.

The pulses generated from the RFSoc pass through a room-temperature amplifier (Minicircuits CMA-83LN+) and a series of attenuators at various temperature stages of a Bluefors LD400 dilution refrigerator. The signal reaches the waveguide input port at base temperature (typically < 10 mK) and interacts with the sample (Fig. 10). The output signal from the waveguide is collected using a readout SMA pin that then passes through a cryogenic circulator, HEMT (High Electron Mobility Transistor) amplifier, and two room-temperature amplifiers (Minicircuits CMA-83LN+), before returning to the RFSoc. A detailed wiring diagram is provided in Fig. 10.

[1] R. C. Zeller and R. O. Pohl, Phys. Rev. B **4**, 2029 (1971).

[2] P. W. Anderson, B. I. Halperin, and C. M. Varma, Philos. Mag. **25**, 1 (1972).

[3] W. A. Phillips, J. Low Temp. Phys. **7**, 351 (1972).

[4] C. Müller, J. H. Cole, and J. Lisenfeld, Rep. Prog. Phys. **82**, 124501 (2019).

[5] W. Arnold and S. Hunklinger, Solid State Commun. **17**, 883 (1975).

[6] B. Golding and J. E. Graebner, Phys. Rev. Lett. **37**, 852 (1976).

[7] J. E. Graebner and B. Golding, Phys. Rev. B **19**, 964 (1979).

[8] J. L. Black and B. I. Halperin, Phys. Rev. B **16**, 2879 (1977).

[9] P. Hu and L. R. Walker, Solid State Commun. **24**, 813 (1977).

[10] M. Carroll, S. Rosenblatt, P. Jurcevic, I. Lauer, and A. Kandala, npj Quantum Inf. **8**, 132 (2022).

[11] J. H. Béjanin, C. T. Earnest, A. S. Sharafeldin, and M. Mariantoni, Phys. Rev. B **104**, 094106 (2021).

[12] C. Wang, C. Axline, Y. Y. Gao, T. Brecht, Y. Chu, L. Frunzio, M. H. Devoret, and R. J. Schoelkopf, Appl. Phys. Lett. **107**, 162601 (2015).

[13] A. P. Read, B. J. Chapman, C. U. Lei, J. C. Curtis, S. Ganjam, L. Krayzman, L. Frunzio, and R. J. Schoelkopf, Phys. Rev. Appl. **19**, 034064 (2023).

[14] D. M. Pozar, *Microwave engineering*, 4th ed. (Wiley, Hoboken, NJ, 2012).

[15] M. D. Reed, B. R. Johnson, A. A. Houck, L. DiCarlo, J. M. Chow, D. I. Schuster, L. Frunzio, and R. J. Schoelkopf, Appl. Phys. Lett. **96**, 203110 (2010).

[16] E. M. Purcell, H. C. Torrey, and R. V. Pound, Phys. Rev. **69**, 37 (1946).

[17] J. Lisenfeld, C. Müller, J. H. Cole, P. Bushev, A. Lukashenko, A. Shnirman, and A. V. Ustinov, Phys. Rev. Lett. **105**, 230504 (2010).

[18] G. J. Grabovskij, T. Peichl, J. Lisenfeld, G. Weiss, and A. V. Ustinov, Science **338**, 232 (2012).

[19] J. Lisenfeld, G. J. Grabovskij, C. Müller, J. H. Cole, G. Weiss, and A. V. Ustinov, Nat. Commun. **6**, 6182 (2015).

[20] J. Lisenfeld, C. Müller, J. H. Cole, P. Bushev, A. Lukashenko, and A. V. Ustinov, npj Quantum Inf. **5**, 105 (2019).

[21] L. Yu, S. Matityahu, Y. J. Rosen, C.-C. Hung, A. Maksymov, A. L. Burin, M. Schechter, and K. D. Osborn, Sci. Rep. **12**, 16960 (2022).

[22] G. S. MacCabe, H. Ren, J. Luo, J. D. Cohen, H. Zhou, A. Sipahigil, M. Mirhosseini, and O. Painter, Science **370**, 840 (2020).

[23] K. D. Crowley, R. A. McLellan, A. Dutta, N. Shumiya, A. P. M. Place, X. H. Le, Y. Gang, T. Madhavan, M. P. Bland, R. Chang, N. Khedkar, Y. C. Feng, E. A. Umbarkar, X. Gui, L. V. H. Rodgers, Y. Jia, M. M. Feldman, S. A. Lyon, M. Liu, R. J. Cava, A. A. Houck, and N. P. de Leon, Phys. Rev. X **13**, 041005 (2023).

[24] P. Chiappina, J. Banker, S. Meesala, D. Lake, S. Wood, and O. Painter, Opt. Express **31**, 22914 (2023).

[25] M. Chen, J. C. Owens, H. Putterman, M. Schäfer, and O. Painter, Sci. Adv. **10**, eado6240 (2024).

[26] M. P. Bland, F. Bahrami, J. G. C. Martinez, P. H. Prestegard, B. M. Smitham, A. Joshi, E. Hedrick, A. Pakpour-Tabrizi, S. Kumar, A. Jindal, R. D. Chang, A. Yang, G. Cheng, N. Yao, R. J. Cava, N. P. de Leon, and A. A. Houck, 2d transmons with lifetimes and coherence times exceeding 1 millisecond (2025), arXiv:2503.14798 [quant-ph].

[27] J. Gao, M. Daal, A. Vayonakis, S. Kumar, J. Zmuidzinas, B. Sadoulet, B. A. Mazin, P. K. Day, and H. G. Leduc, Appl. Phys. Lett. **92**, 152505 (2008).

[28] G. Calusine, A. Melville, W. Woods, R. Das, C. Stull, V. Bolkhovsky, D. Braje, D. Hover, D. K. Kim, X. Miloshi, D. Rosenberg, A. Sevi, J. L. Yoder, E. A. Dauler, and W. D. Oliver, Appl. Phys. Lett. **112**, 062601 (2018).

[29] W. Woods, G. Calusine, A. Melville, A. Sevi, E. Golden, D. K. Kim, D. Rosenberg, J. L. Yoder, and W. D. Oliver, Phys. Rev. Appl. **12**, 014012 (2019).

[30] C. R. H. McRae, H. Wang, J. Gao, M. R. Vissers, T. Brecht, A. Dunsworth, D. P. Pappas, and J. Mutus, Rev. Sci. Instrum. **91**, 091101 (2020).

[31] C.-C. Hung, L. Yu, N. Foroozani, S. Fritz, D. Gerthsen, and K. D. Osborn, Phys. Rev. Appl. **17**, 034025 (2022).

[32] J. M. Martinis, K. B. Cooper, R. McDermott, M. Steffen, M. Ansmann, K. D. Osborn, K. Cicak, S. Oh, D. P. Pappas, R. W. Simmonds, and C. C. Yu, Phys. Rev. Lett. **95**, 210503 (2005).

[33] J. Burnett, L. Faoro, I. Wisby, V. L. Gurtovoi, A. V. Chernykh, G. M. Mikhailov, V. A. Tulin, R. Shaikhaidarov, V. Antonov, P. J. Meeson, A. Y. Tzalenchuk, and T. Lindström, Nat. Commun. **5**, 4119 (2014).

[34] C. Müller, J. Lisenfeld, A. Shnirman, and S. Poletto, Phys. Rev. B **92**, 035442 (2015).

[35] A. Agarwal, L. P. Lindoy, D. Lall, F. Jamet, and I. Rungger, Quantum Sci. Technol. **9**, 035017 (2024).

[36] M. Odeh, K. Godeneli, E. Li, R. Tangirala, H. Zhou, X. Zhang, Z.-H. Zhang, and A. Sipahigil, Nat. Phys. **21**, 406 (2025).

[37] M. Spiecker, A. I. Pavlov, A. Shnirman, and I. M. Pop, Phys. Rev. A **109**, 052218 (2024).

[38] C. Macklin, K. O'Brien, D. Hover, M. E. Schwartz, V. Bolkhovsky, X. Zhang, W. D. Oliver, and I. Siddiqi, Science **350**, 307 (2015).

[39] M. Boselli, J. Grebel, A. Peugeot, R. Dassonneville, B. Huard, and A. Bienfait, Observation and mitigation of microwave echoes from dielectric defects in josephson traveling wave amplifiers (2025), arXiv:2503.00190 [quant-ph].

[40] A. Delattre, I. Golokolenov, R. Pedurand, N. Roch, A. Ranadive, M. Esposito, L. Planat, A. Fefferman, E. Collin, X. Zhou, M. A. Sillanpää, L. Mercier de Lepinay, A. D. Armour, and J. Glatthard, Quantitative calibration of a TWPA applied to an optomechanical platform (2025), arXiv:2505.05837 [quant-ph].

[41] A. M. Holder, K. D. Osborn, C. J. Lobb, and C. B. Musgrave, Phys. Rev. Lett. **111**, 065901 (2013).

[42] A. Megrant and Y. Chen, Nature Electronics **1** (2025).

[43] M. Thorwart, M. Grifoni, and P. Hänggi, Phys. Rev. Lett. **85**, 860 (2000).

[44] R. Kubo, J. Phys. Soc. Jpn. **12**, 570 (1957).

[45] C. W. Gardiner and M. J. Collett, Phys. Rev. A **31**, 3761

(1985).

[46] L. Novotny, M. Frimmer, A. Militaru, A. Norrman, O. Romero-Isart, and P. Maurer, *Phys. Rev. A* **106**, 043511 (2022).

[47] L. Stefanazzi, K. Treptow, N. Wilcer, C. Stoughton, C. Bradford, S. Uemura, S. Zorzetti, S. Montella, G. Cancelo, S. Sussman, A. Houck, S. Saxena, H. Arnaldi, A. Agrawal, H. Zhang, C. Ding, and D. I. Schuster, *Rev. Sci. Instrum.* **93**, 044709 (2022).

[48] K. D. Crowley, R. A. McLellan, A. Dutta, N. Shumiya, A. P. M. Place, X. H. Le, Y. Gang, T. Madhavan, M. P. Bland, R. Chang, N. Khedkar, Y. C. Feng, E. A. Umbarkar, X. Gui, L. V. H. Rodgers, Y. Jia, M. M. Feldman, S. A. Lyon, M. Liu, R. J. Cava, A. A. Houck, and N. P. De Leon, *Phys. Rev. X* **13**, 041005 (2023).

[49] J. Lisenfeld, C. Müller, J. H. Cole, P. Bushev, A. Lukashenko, A. Shnirman, and A. V. Ustinov, *Phys. Rev. Lett.* **105**, 230504 (2010).

[50] A. P. M. Place, L. V. H. Rodgers, P. Mundada, B. M. Smitham, M. Fitzpatrick, Z. Leng, A. Premkumar, J. Bryon, A. Vrajitoarea, S. Sussman, G. Cheng, T. Madhavan, H. K. Babla, X. H. Le, Y. Gang, B. Jäck, A. Gynnis, N. Yao, R. J. Cava, N. P. de Leon, and A. A. Houck, *Nat. Commun.* **12**, 1779 (2021).

[51] S. Sangtawesin, B. L. Dwyer, S. Srinivasan, J. J. Allred, L. V. H. Rodgers, K. De Greve, A. Stacey, N. Dontschuk, K. M. O'Donnell, D. Hu, D. A. Evans, C. Jaye, D. A. Fischer, M. L. Markham, D. J. Twitchen, H. Park, M. D. Lukin, and N. P. de Leon, *Phys. Rev. X* **9**, 031052 (2019).

[52] M. W. Olszewski, J. T. Paustian, T. Banerjee, H. Lu, J. L. Ramirez, N. Nguyen, K. Okubo, R. Pant, A. B. Biedron, D. C. Ralph, C. J. K. Richardson, G. D. Fuchs, C. R. H. McRae, I. V. Pechenezhskiy, B. L. T. Plourde, and V. Fatemi, Low-loss nb on si superconducting resonators from a dual-use spintronics deposition chamber and with acid-free post-processing (2025), arXiv:2503.13285 [quant-ph].

[53] C. Gaikwad, D. Kowsari, C. Brame, X. Song, H. Zhang, M. Esposito, A. Ranadive, G. Cappelli, N. Roch, E. M. Levenson-Falk, and K. W. Murch, *Phys. Rev. Lett.* **132**, 200401 (2024).

[54] R. D. Chang, N. Shumiya, R. A. McLellan, Y. Zhang, M. P. Bland, F. Bahrami, J. Mun, C. Zhou, K. Kisslinger, G. Cheng, B. M. Smitham, A. C. Pakpour-Tabrizi, N. Yao, Y. Zhu, M. Liu, R. J. Cava, S. Gopalakrishnan, A. A. Houck, and N. P. de Leon, *Phys. Rev. Lett.* **134**, 097001 (2025).

[55] C. M. Quintana, A. Megrant, Z. Chen, A. Dunsworth, B. Chiaro, R. Barends, J. Kelly, J. Mutus, D. Sank, J. Wenner, Y. Yin, J. Zhao, A. N. Cleland, and J. M. Martinis, *Appl. Phys. Lett.* **105**, 062601 (2014).

[56] B. Lévi, C. C. López, J. Emerson, and D. G. Cory, *Phys. Rev. A* **75**, 022314 (2007).

[57] A. K. Jonscher, *Nature* **267**, 673 (1977).

[58] A. Jonscher, *IEEE Trans. Electr. Insul.* **27**, 407 (1992).

[59] E.-M. Laine, J. Pilo, and H.-P. Breuer, *Phys. Rev. A* **81**, 062115 (2010).

[60] A. Rivas, S. F. Huelga, and M. B. Plenio, *Phys. Rev. A* **83**, 052128 (2011).

[61] M. S. Kumar and G. S. Agarwal, *Phys. Rev. A* **33**, 1817 (1986).

[62] M. M. Ali, P.-Y. Lo, M. W.-Y. Tu, and W.-M. Zhang, *Phys. Rev. A* **92**, 062306 (2015).

[63] G. Busiello, *J. Mod. Phys.* **04**, 784 (2013).

[64] F. Castles, J. A. J. Fells, D. Isakov, S. M. Morris, A. A. R. Watt, and P. S. Grant, *Adv. Mater.* **32**, 1904863 (2020).

[65] B. M. Terhal and G. Burkard, *Phys. Rev. A* **71**, 012336 (2005).

[66] P. W. Shor, in *Proceedings of the 37th Annual Symposium on Foundations of Computer Science (FOCS)* (1996) pp. 56–65.

[67] L. Stefanazzi, K. Treptow, N. Wilcer, C. Stoughton, C. Bradford, S. Uemura, S. Zorzetti, S. Montella, G. Cancelo, S. Sussman, A. Houck, S. Saxena, H. Arnaldi, A. Agrawal, H. Zhang, C. Ding, and D. I. Schuster, *Rev. Sci. Instrum.* **93**, 044709 (2022).

ACKNOWLEDGMENTS

Bert Harrop graciously diced the devices at Princeton. Simon Agnew helped perform the aluminum oxide deposition using an atomic layer deposition tool in William Scheideler's lab at Dartmouth. We also acknowledge stimulating conversations with Kater Murch, Miles Blencowe, Geoffroy Hautier, Chandrasekhar Ramanathan, and Valla Fatemi. Startup funds from the Thayer School of Engineering at Dartmouth primarily supported this work. While the scientific focus of this work is quite distinct from existing funding, M.F. would like to express gratitude for the support of science within his group through the DARPA Young Faculty Award No. D23AP00192 and NSF PHY-2412555, and hopes that projects like this continue to be made possible by grants from the US federal government. The views and conclusions in this manuscript are those of the authors. They should not be interpreted as representing the official policies, expressed or implied, of DARPA, the NSF, or the US Government. The US Government is authorized to reproduce and distribute reprints for Government purposes, notwithstanding any copyright notation herein.

AUTHOR CONTRIBUTIONS

M.F. proposed the waveguide approach and guided the experimental and theoretical work. Q.W. performed the experiments, made the figures, and developed the data analysis pipeline for this work. S.M.G. and J.F. designed and fabricated the waveguide. J.S.S.G., R.L., and S.B. provided theoretical support. J.S.S.G., S.B., and M.F. provided context for the work. S.B. provided theoretical insights using an interacting-driven TLS model to validate the observed patterns. All authors jointly validated the results and participated in the writing of the manuscript.

COMPETING INTERESTS

The authors declare no competing interests.

ADDITIONAL INFORMATION**Correspondence and request for materials**

Correspondence and material requests should be directed to Mattias Fitzpatrick (mat-

tias.w.fitzpatrick@dartmouth.edu). Data supporting the findings of this study are available from the corresponding author upon reasonable request.